Journal of Materials Chemistry B

ROYAL SOCIETY OF CHEMISTRY

PAPER

View Article Online
View Journal | View Issue

Cite this: *J. Mater. Chem. B*, 2021, **9**, 2001

Nanoscale photosensitizer with tumor-selective turn-on fluorescence and activatable photodynamic therapy treatment for COX-2 overexpressed cancer cells†

Lan Wang, Yuhuan Zhang, Ying Han, Qi Zhang, Zhenfu Wen, Hongjuan Li, Shiguo Sun, Xin Chen and Yongqian Xu *

Received 5th December 2020,
Accepted 21st January 2021

DOI: 10.1039/d0tb02828b

rsc.li/materials-b

Effective targeting and *in situ* imaging-guided treatment are particularly important for accurate clinical photodynamic therapy (PDT) of malignant tumors. Herein, we propose a single molecule, named **IMC-DAH-SQ**, which possesses dual-targeting components, including structure-inherent targeting (SIT) and cyclooxygenase-2 (COX-2) targeting units, and controllable turn-on near infrared (NIR) fluorescence. Due to its amphiphilicity, **IMC-DAH-SQ** assembles into a nanoprobe with low background fluorescence. After incubation with tumor cells, the SIT and COX-2 recognition characteristics of **IMC-DAH-SQ** endow it with preferential tumor-targeting activity. The strong binding with overexpressed COX-2 can collapse the nanoprobe to monomers after accumulation in tumor cells, leading to turn-on NIR fluorescence that is completely different from normal cells. Additionally, benefiting from the single molecular model tactic, the nanoprobe has the advantages of simple synthesis without ever considering the loading rate and separation between the photosensitizer and targeting unit. Other favorite features, including superior biocompatibility, weak dark toxicity, and mitochondria enrichment capability, are implemented. All these traits not only afford nanoprobe precision tumor cell targeting capability but also provide promising imaging-guided antitumor therapy. We believe that the single molecular protocol will establish a novel strategy for simultaneous diagnosis and anticancer medicine treatment utilizing versatile but small compounds.

Introduction

Photodynamic therapy (PDT) has become a promising treatment modality because of its noninvasiveness, small side effects and no drug resistance.[1] PDT relies on photosensitizers and excitation light to produce cytotoxic reactive oxygen species (ROS) to kill cancer cells.[2] However, ROS are non-targetable and have a short lifetime; therefore, photosensitizers must be enriched in the tumor site to improve the PDT effect availably and to reduce side effects. To achieve targeting capability of photosensitizers, strategies such as the bioconjugation of photosensitizers with target ligands have been widely utilized.[3,4] However, the conjugated molecular synthesis is time-consuming and laborious, and the separation of the photosensitizer and targeting unit and a low loading rate of the photosensitizer are unavoidable. As an ideal alternative, integrating multiple targeting and tumor environment-activated mechanisms into a single molecule without carrier delivery could improve the accuracy and efficiency of recognition and minimize the side effects of PDT. Due to the unique and fast metabolism, the membrane of tumor cells possesses more negative charge than normal cells, leading them to absorb and swallow positively charged molecules preferentially.[5–8] Structure-inherent targeting (SIT) provides a new opportunity to achieve targetable delivery. In the past, SIT was mainly used for biological imaging; it has rarely been used for tumor-targetable delivery.[9]

Cyclooxygenase-2 (COX-2) is closely related to the growth of various stages of cancer; it is overexpressed in tumor cells and has become a specific biomarker of tumor cells.[10] As an inhibitor of COX-2, indomethacin (IMC) can closely interact with COX-2; also, due to the high affinity between IMC and COX-2, IMC is a useful ligand for tumor targeting.[11] Mitochondria, the powerhouse of cells, regulates the growth and metabolism of cells.[12] The dysfunction of mitochondria can easily lead to the death of cells.[13] If PDT photosensitizers can target and accumulate in the mitochondria of tumor cells, they can subsequently produce

Shaanxi Key Laboratory of Natural Products & Chemical Biology, College of Chemistry & Pharmacy, Northwest A&F University, Yangling, Shaanxi, 712100, P. R. China. E-mail: xuyq@nwsuaf.edu.cn

† Electronic supplementary information (ESI) available: Additional spectra such as zeta potential distribution, cell viability, fluorescent imaging in cells and NMR spectra of compounds. See DOI: 10.1039/d0tb02828b

toxic ROS, which would significantly promote the killing of cancer cells.[14,15] Thus, undoubtedly searching for photosensitizers targeting the mitochondria of tumor cells is beneficial to improve the PDT efficiency.

Among many biological imaging technologies, fluorescence imaging has become a useful tool because of its high sensitivity, real-time imaging with high spatial resolution, noninvasiveness, *etc.* PDT that is accompanied by the fluorescence imaging of tumor cells in the whole process, called imaging-guided PDT, can visually control and effectively improve the effects of PDT by limiting the light range and reducing the phototoxicity.[16] Therefore, ideal PDT photosensitizers should have good biocompatibility, low dark toxicity and high singlet oxygen production, and they can be used for imaging-guided PDT with NIR fluorescence.[17] Although the existing photosensitizers, mainly including porphyrin, phthalocyanines, BODIPY, and aggregation-induced emission (AIE) dyes,[18] have been widely used in imaging-guided PDT, their "always-on" signal characteristics are not conducive to distinguishing tumor cells from normal cells. Moreover, they do not have the ability to only produce ROS in tumor cells and not in normal cells. Therefore, it is still challenging to develop photosensitizers that meet all the above requirements.

Herein, we report a small molecule, **IMC-DAH-SQ**, which can be easily synthesized as a PDT reagent (Scheme 1). It has a tumor cell targeting function *via* SIT and interacts with COX-2. Meanwhile, the tumor cell-induced turn-on fluorescence imaging can be used for recognition and possible imaging-guided PDT. Specifically, we connected IMC and a NIR fluorescence squaraine (SQ) dye through a short flexible chain. This simple connection avoids the separation of the photosensitizer and the recognition unit, and it ensures a high loading rate of the photosensitizer. The positively charged feature of SQ endows **IMC-DAH-SQ** with preferential access to tumor cells *via* SIT.[19] Due to the amphiphilicity, **IMC-DAH-SQ** can aggregate in aqueous solution to form nano-photosensitizers. The nanoscale architecture endows **IMC-DAH-SQ** with a low background fluorescence signal due to the aggregation-caused quenching (ACQ) characteristic of SQ (Scheme 1). The molecular self-assembly system of **IMC-DAH-SQ** inhibits fluorescence emission and ROS generation. After accumulation in tumor cells, the binding of IMC with COX-2 disperses the nanoprobe into the monomer. Obvious NIR fluorescence appears in the tumor, which can be utilized for the fluorescence recognition of tumor cells. Due to the positive charge of **IMC-DAH-SQ**, it further targets the mitochondria. As a promising photosensitizer, SQ can produce singlet oxygen in mitochondria under excitation. PDT-induced ablation was especially triggered in tumor cells. This multifunctional and intelligent molecule with carrier-free delivery can realize high selectivity and good efficiency of PDT of tumor cells.

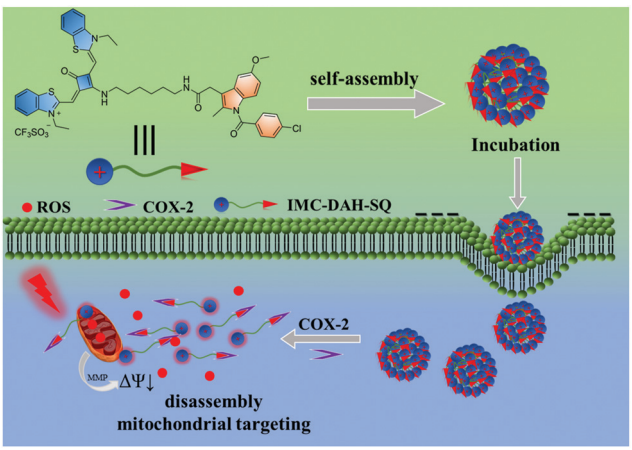

Scheme 1 The structure of **IMC-DAH-SQ** and the cascade processes of aggregation, disaggregation, lighting up and ROS production of **IMC-DAH-SQ**.

Experimental

Materials

The chemical reagents used here were purchased from Energy Chemical Reagents Co. and Mayer Chemical Reagents Co. (Shanghai, China). All these reagents were used as received without further purification unless otherwise stated. The water used was ultrafilter deionized. The Live-Dead cell staining kit was purchased from Yeasen Biotech Co., Ltd (Shanghai, China). The mitochondrial membrane potential fluorescent probe JC-1 was purchased from Solarbio Science & Technology Co., Ltd (Beijing, China).

General methods

^{1}H NMR and ^{13}C NMR data were obtained from a Bruker AVANCE III 500 spectrometer (Germany) (NMR data were referenced to TMS used as the internal standard). Mass spectra were obtained with an LCQ Fleet mass spectrometer (USA) and an AB SCIEX LC-30A + TripleTOF5600 + mass spectrometer (Singapore). Fluorescence spectra and UV-Vis spectra were carried out on a RF-6000 fluorescence spectrometer and a Shimadzu 1750 UV-visible spectrometer (Japan), respectively. Confocal fluorescence imaging of cells was performed using an Olympus FV1000MPE laser scanning confocal microscope (Japan). Dynamic light scattering (DLS) and zeta potential were performed with a Malvern Instruments Limited ZEN3600 (Britain). The quantum yields of fluorescence of the samples were measured using Rhodamine B in ethanol (Φ = 0.49) as a standard and calculated according to the method below:

$$\Phi_u = \frac{(\Phi_s)(I_u)(A_s)(\lambda_{exs})(\eta_u^2)}{(I_s)(A_u)(\lambda_{exu})(\eta_s^2)}$$

where Φ represents the fluorescence quantum yield. I represents the integrated emission intensities. A is the absorbance at the excitation wavelength. λ_{ex} represents the excitation wavelength. η is the refractive index of the corresponding solution. The subscripts u and s represent the sample and the standard, respectively.

Synthesis of IMC-DAH-Boc

IMC-DAH-Boc was synthesized according to a previously reported method with slight modification.[20] To a 100 mL single-necked flask, IMC (0.59 g, 1.65 mmol), HATU (0.94 g, 2.5 mmol), DAH-Boc (0.425 g, 1.95 mmol), and TEA (0.505 g, 5 mmol) were dissolved in 10 mL DMF. Then, the mixture was

stirred for 4 h at room temperature. After completion of the reaction, the mixture was poured into excess ice water. The precipitate was collected by filtration and dried to obtain the crude compound **IMC-DAH-Boc** as a milk yellow solid, and pure **IMC-DAH-Boc** was obtained by column chromatography (514 mg, 56.05% yield). ^{1}H NMR (500 MHz, $CDCl_3$) δ 7.64 (d, J = 8.5 Hz, 2H), 7.46 (d, J = 8.5 Hz, 2H), 6.86 (m, 2H), 6.67 (dd, J = 9.0, 2.5 Hz, 1H), 5.70 (s, 1H), 4.51 (s, 1H), 3.80 (s, 3H), 3.61 (s, 2H), 3.16 (q, J = 6.5 Hz, 2H), 3.01 (d, J = 6.0 Hz, 2H), 2.36 (s, 3H), 1.42–1.32 (m, 13H), 1.25–1.13 (m, 4H). ESI-MS: m/z calcd for $[M + H]^+$: 578.10, found: 578.26.

Synthesis of IMC-DAH-SQ

SQ was prepared according to the reported literature.[21]

To a 100 mL flask in an ice bath, **IMC-DAH-Boc** (166.8 mg, 0.3 mmol), 5 mL DCM and 5 mL TFA were added in turn. The mixed solution was stirred at room temperature for 10 h and then concentrated by a rotary evaporator. The residue was dissolved with 20 mL ethyl acetate, washed with 5 M NaOH solution (3 × 20 mL) and saturated NaCl solution (2 × 20 mL), dried with anhydrous Na_2SO_4 and concentrated by rotary evaporator to obtain the desired compound IMC-DAH (123 mg, 89.9% yield). The compound IMC-DAH was used directly in the next reaction without further purification. IMC-DAH (123 mg, 0.27 mmol), SQ (130 mg, 0.216 mmol), DMAP (10 mg, 0.08 mmol) and TEA (80 μL, 0.575 mmol) were mixed in 10 mL DCM. The resulting solution was stirred at room temperature for 10 h under nitrogen protection. The mixture was concentrated by a rotary evaporator to afford the crude compound. The crude compound was purified with silica gel column chromatography to obtain a cyanic solid **IMC-DAH-SQ** (67 mg, 30.39% yield). ^{1}H NMR (500 MHz, DMSO-d_6) δ 8.73 (t, J = 5.5 Hz, 1H), 8.06 (t, J = 5.5 Hz, 1H), 7.99 (d, J = 7.5 Hz, 1H), 7.92 (d, J = 8.0 Hz, 1H), 7.70 (d, J = 8.0 Hz, 1H), 7.65–7.58 (m, 5H), 7.54 (d, J = 7.5 Hz, 1H), 7.49 (d, J = 8.0 Hz, 1H), 7.38 (d, J = 8.0 Hz, 1H), 7.33 (d, J = 8.0 Hz, 1H), 7.12 (s, 1H), 6.84 (d, J = 9.0 Hz, 1H), 6.63 (dd, J = 9.0, 2.5 Hz, 1H), 6.18 (s, 1H), 5.76 (s, 1H), 4.31 (q, J = 6.5 Hz, 4H), 3.73 (s, 3H), 3.51 (m, 4H), 3.09 (q, J = 6.5 Hz, 2H), 2.23 (s, 3H), 1.60 (m, 2H), 1.45 (m, 2H), 1.38–1.27 (m, 6H), 1.23 (t, J = 7.0 Hz, 4H). ^{13}C NMR (125 MHz, DMSO-d_6) δ 173.5, 169.3, 167.7, 163.1, 160.9, 159.3, 157.2, 155.6, 155.5, 140.3, 140.2, 137.6, 135.1, 134.2, 131.1, 130.8, 130.2, 129.0, 125.0, 124.5, 123.0, 122.7, 114.5, 114.4, 113.2, 112.8, 111.1, 101.9, 86.2, 86.1, 55.4, 43.5, 41.6, 41.0, 38.4, 31.2, 30.9, 29.2, 25.9, 25.9, 13.4, 12.6, 12.0. TOF MS: m/z calcd for $[M - CF_3SO_3^-]^+$: 870.2909, found: 870.2929.

Molecular modeling

The X-ray crystal structures of COX-2 binding with indomethacin-ethylenediamine-dansyl conjugate (PDB code: 6BL4) was retrieved from the Protein Data Bank. The chemical structure of the nanoprobe **IMC-DAH-SQ** was prepared using the protein preparation wizard in Maestro with standard settings. The grids of COX-2 were generated using Glide version 10.2, following the standard procedure recommended by Schrodinger. The conformational ensembles were docked flexibly using Glide with standard settings in both standard and extra precision modes. Only poses with low energy conformations and good hydrogen-bond geometries were considered. Molecular-protein docking results and small-molecule-protein co-crystal structures were shown using Pymol.[22]

Cell viability assay

The cell viabilities of HepG2 and HL7702 cells were evaluated by 3-(4,5-dimethythiazol-2-yl)-2,5-diphenyltetrazolium bromide (MTT) assays. In short, the different cell lines were seeded in 96-well plates (NEST) with an intensity of 8×10^4 cells per mL, respectively. After 24 h incubation, the medium was replaced with **IMC-DAH-SQ** solution with different concentrations (0–20 μM in 1% DMSO). Incubation continued for 24 h at 37 °C; then, the medium of **IMC-DAH-SQ** solution was removed and incubation continued for certain time intervals in fresh RPMI-1640 at 37 °C. After that, the cells were washed twice with PBS buffer, and 100 μL freshly prepared MTT solution (0.5 mg mL^{-1}) was added. After 4 h, the MTT solution was removed and 100 μL DMSO was added to each well. Then, the plate was gently shaken to dissolve the precipitates produced. The absorbance of MTT at 490 nm was measured by a microplate reader.

Cell imaging

Cancer cell lines (HepG2, A549, MCF-7) and normal cell lines (HL7702 and 293T) were seeded on 35 mm glass-bottomed dishes (NEST) with culture medium at 37 °C and incubated for 24 h. The culture medium was carefully removed, and the cells were further incubated with 1 mL **IMC-DAH-SQ** (5 μM) medium solution at room temperature for 0.5 h. Then, the excess nanoprobe was removed by washing with PBS buffer three times, and the obtained cells were imaged.

Inhibitor control experiment

HepG2, A549 and MCF-7 cells were seeded on 35 mm glass-bottomed dishes (NEST) and incubated in culture medium at 37 °C for 24 h. The cells were pretreated with 50 μM inhibitor indomethacin and celecoxib at 37 °C for 16 h. The unabsorbed inhibitor was carefully removed by washing with PBS buffer three times. Then, the cells were incubated with 5 μM **IMC-DAH-SQ** for 0.5 h at room temperature and washed with PBS buffer before imaging.

Lipopolysaccharide up-regulates the COX-2 level

HL7702 and 293T cells were seeded on 35 mm glass-bottomed dishes (NEST) and incubated in culture medium at 37 °C for 24 h. The cells were pretreated with 1 mg mL^{-1} lipopolysaccharide (LPS) at 37 °C for 24 h. The unabsorbed LPS was carefully removed by washing with PBS buffer three times, and the cells were further incubated with 5 μM **IMC-DAH-SQ** for 0.5 h at room temperature and washed with PBS buffer before imaging.

Co-localization experiment

HepG2 cells were seeded on 35 mm glass-bottomed dishes (NEST) and incubated in culture medium at 37 °C for 24 h. The cells were pretreated with 5 μM **IMC-DAH-SQ** and Rhodamine 123 at room temperature for 0.5 h. The excess nanoprobe

and Rhodamine 123 were carefully removed by washing with PBS three times before imaging.

In vitro ROS detection

9,10-Anthracenediyl-bis(methylene)dimalonic acid (ABDA) was employed to detect ROS *in vitro*. The typical procedure for detection of ROS is as follows: **IMC-DAH-SQ** and 50 μM ABDA were mixed in DMSO in a cuvette. Then, the solution was irradiated with a 630 nm LED lamp (25 mW cm^{-2}) at room temperature.

Determination of the ROS quantum yield

For the ROS quantum yield (Φ) measurement, 1,3-diphenylbenzofuran (DPBF) was used as a probe, and methylene blue (MB, Φ = 0.52 in DMSO) was used as the reference. The mixture solutions were irradiated at 630 nm (25 mW cm^{-2}) for 60 min. The absorbance of the solutions was measured for different periods of time. The following equation was used to calculate the ROS quantum yield:[23]

$$\Phi = \Phi(\mathrm{MB})\frac{m(\mathrm{PS})}{m(\mathrm{MB})}\frac{F(\mathrm{MB})}{F(\mathrm{PS})}\frac{P(\mathrm{MB})}{P(\mathrm{PS})}$$

where m is the slope of the absorption change of DPBF at 415 nm against the irradiation time. F is the absorption correction factor, which is given as $F = 1 - 10^{-\mathrm{OD}}$. P is the absorbed photonic flux.

Intracellular ROS detection

HepG2 cells were seeded on 35 mm glass-bottomed dishes (NEST) and incubated in culture medium at 37 °C for 24 h. The cells were pretreated with 5 μM **IMC-DAH-SQ** at room temperature for 0.5 h. The unabsorbed nanoprobe was carefully removed by washing with PBS buffer three times, and the cells were further incubated with DCFH-DA in fresh culture medium for 0.5 h at room temperature. After that, the glass-bottomed dishes were irradiated with a 630 nm LED light for 12.5 min at a power density of 20 mW cm^{-2}. Then, the cells were imaged by a fluorescence confocal microscope.

Mitochondrial membrane potential detection

HepG2 cells were seeded on 35 mm glass-bottomed dishes (NEST) and incubated in culture medium at 37 °C for 24 h. The cells were pretreated with different concentrations of **IMC-DAH-SQ** at 37 °C for 4 h. Then, the cells were irradiated with a 630 nm LED light for 12.5 min at a power density of 20 mW cm^{-2} and further incubated for 24 h. The mitochondrial membrane potential probe JC-1 was used according to the instructions.

Photodynamic therapy *in vitro*

Cancer cells HepG2 in 96-well plates (NEST) were seeded with culture medium at 37 °C and incubated for 24 h. Fresh medium with **IMC-DAH-SQ** was used to replace the culture medium, followed by incubation at 37 °C for 0.5 h. Then, the cells were irradiated with a 630 nm LED light for 12.5 min at a power density of 25 mW cm^{-2} and further incubated for 24 h. For detection of the cell viability, MTT assays were carried out.

Calcein-AM/PI staining experiment

HepG2 cells were seeded on 35 mm glass-bottomed dishes (NEST) and incubated in culture medium at 37 °C for 24 h. Then, the cells were pretreated with different concentrations of **IMC-DAH-SQ** at 37 °C for 4 h. The glass-bottomed dishes were irradiated with a 630 nm LED light for 12.5 min at a power density of 25 mW cm^{-2} and further incubated for 24 h. A Calcein-AM/PI Double Stain Kit was used according to the instructions.

Flow cytometry

Cells were gathered in each group, centrifuged for 5 min, and washed twice with PBS. 1–10 × 10^5 cells were suspended in PBS. In the assay, cell death was detected by the Annexin V-EGFP/PI Apoptosis Detection Kit (Yeasen Biotechnology Co., Ltd China). In short, HepG2 cells treated with **IMC-DAH-SQ** were suspended in 100 mL buffer mixed with 5 mL propidium iodide (PI) and 5 mL Annexin V-EGFP, incubated at room temperature for 20 min in the dark, and detected *via* flow cytometer (BD Biosciences, FACA CA, USA). The flow cytometry was qualified within 1 h after the dye solution was added.

Results and discussion

Photophysical properties of IMC-DAH-SQ

The synthesis and detailed characterization of **IMC-DAH-SQ** are listed in the ESI† (Scheme S1 and Fig. S10–S16). The spectra of IMC-DAH-SQ in different solutions were studied (Table S1, ESI†). For the emission spectra, IMC-DAH-SQ has a strong NIR fluorescence peak in DMSO solution and a weak one in aqueous solution (Fig. 1a). The weak fluorescence intensity in aqueous solution can be attributed to ACQ, affording low background fluorescence of IMC-DAH-SQ. As shown in Fig. 1b and Table S1 (ESI†), IMC-DAH-SQ showed an absorption peak in organic solutions. In aqueous solution, IMC-DAH-SQ demonstrated two prominent absorption peaks at 654 and 607 nm, assigned to the monomer and aggregates. To check the morphology of the IMC-DAH-SQ aggregates in aqueous solution, scanning electron microscopy (SEM) and dynamic light scattering (DLS) spectroscopy were performed. Regular and spherical nanoparticles with sizes in the range of 130–150 nm were found (Fig. 2), supporting the formation of the IMC-DAH-SQ nanoprobe. The surface zeta potential of the IMC-DAH-SQ nanoparticles is

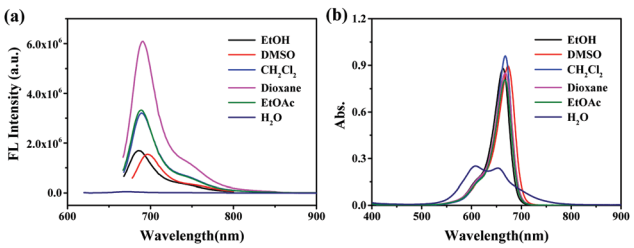

Fig. 1 (a) Emission spectra and (b) UV-vis absorption spectra of **IMC-DAH-SQ** (5 μM) in different solutions.

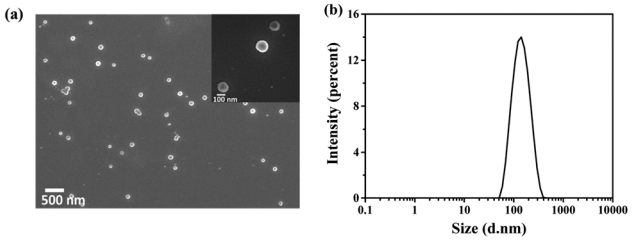

Fig. 2 (a) SEM image and (b) DLS spectra of **IMC-DAH-SQ** nanoparticles formed in aqueous solution.

37.8 mV (Fig. S1, ESI†). The markedly positive feature endows the **IMC-DAH-SQ** nanoprobe with SIT capability to access cancer cells.[24]

The fluorescence quenching mechanism and binding mode of IMC-DAH-SQ with COX-2

Gaussian 16 (DFT at the B3LYP/6-311G(d) level) was used to calculate the frontier molecular orbital (FMO) energies of **IMC-DAH-SQ** (Fig. S2, ESI†). The oscillator strength from the HOMO (S0) to the LUMO (S1) is about 1.49 and is unchanged from folded to unfolded **IMC-DAH-SQ**. Therefore, there is no photo-induced electron transfer (PET) process in **IMC-DAH-SQ** because electron transition from the HOMO (S0) to the LUMO (S1) is possible.[24] The low fluorescence of **IMC-DAH-SQ** in water is attributed to the aggregation and is in contrast to the good fluorescence quantum yields in organic solvents (Fig. 1a).

To verify whether the introduction of SQ into IMC affects the interaction between IMC and COX-2 and to understand the underlying interaction model between **IMC-DAH-SQ** and COX-2, molecular model calculations were used to study the possible binding mode. According to the calculation results, the recognition group IMC of **IMC-DAH-SQ** inserts into the COX-2 side pocket, which is composed of amide groups of Y385, S350, S353, Y355, A527, R120 and S119 (Fig. 3). We compared the binding mode with that between reported compound **1** and COX-2.[22] Referenced compound **1**, featuring the same recognition group as **IMC-DAH-SQ** and a similar chemical structure, has a good interaction with COX-2. As shown in Fig. 3, both compound **1** and **IMC-DAH-SQ** form hydrogen bonds with Y355 and R120 of COX-2. The interactions of **IMC-DAH-SQ** and compound **1** with COX-2 are similar to a great extent (Fig. 3b). Moreover, the long alkyl chain of **IMC-DAH-SQ** prefers to arrange along the gap of COX-2, by which the photosensitizer SQ is effectively exposed. As a result, the interaction between **IMC-DAH-SQ** and COX-2 could collapse the aggregates to release the monomers, restoring the fluorescence signal inhibited by aggregation.

Cellular uptake imaging

Biological toxicity is a significant criterion for cancer detection; the dark cytotoxicity of **IMC-DAH-SQ** to HepG2 and HL7702 cells was evaluated *via* the MTT test. After incubation for 24 h, the experimental results demonstrated that **IMC-DAH-SQ** has no obvious cytotoxicity in live HepG2 and HL7702 cells (Fig. S3,

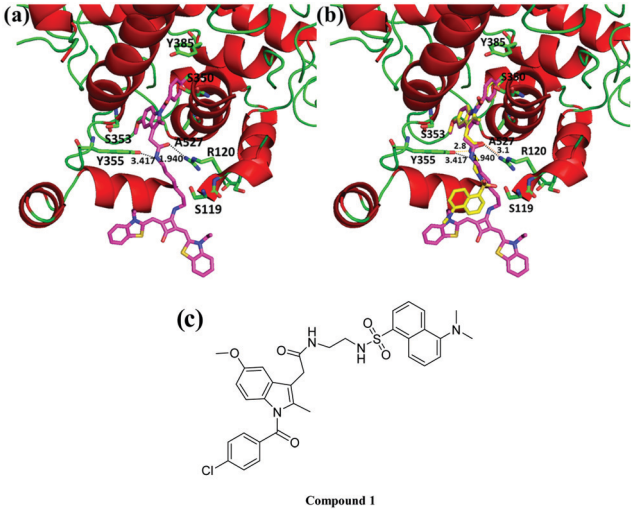

Fig. 3 (a) Stereoview of the molecular interaction between **IMC-DAH-SQ** and COX-2; (b) overlay model of **IMC-DAH-SQ** and compound **1** binding with COX-2. (c) Chemical structures of **IMC-DAH-SQ** and compound **1**. **IMC-DAH-SQ** is colored purple and compound **1** is colored yellow. Referenced compound **1** featuring the same recognition group as **IMC-DAH-SQ** and a similar chemical structure, has good interaction with COX-2. For **IMC-DAH-SQ**, the hydrogen bond distance between Y355 and the nitrogen atom of the amide neighboring indomethacin part is 3.4 Å, and the hydrogen bond distance between NH_2 in the guanidine group of R120 and the carbonyl oxygen of the amide group of **IMC-DAH-SQ** is 1.9 Å. For compound **1**, the corresponding hydrogen bond distances are 3.1 and 2.8 Å, respectively.

ESI†). To evaluate the ability of **IMC-DAH-SQ** to specifically target COX-2, we treated different cancer cells (MCF-7, A549 and HepG2) and normal cells (293T and HL7702) with the nanoprobe **IMC-DAH-SQ**. The interaction between **IMC-DAH-SQ** and excess COX-2 in cancer cells through special binding of IMC with COX-2 can disaggregate the nanoprobe **IMC-DAH-SQ**, lighting up cancer cells with NIR fluorescence (Fig. S4, ESI†). As shown in Fig. 4A, after incubation with the nanoprobe **IMC-DAH-SQ**, the cancer cell lines showed a strong fluorescence signal, while the normal cell lines displayed a negligible fluorescence signal. As depicted in Fig. 4B, the fluorescence intensity in cancer cells was 18.2-fold larger than that in normal cells, revealing the de-aggregation by COX-2. This fact can be attributed to the specific binding of the IMC unit with overexpressed COX-2 in cancer cells.[25] In addition, the positively charged nanoprobe **IMC-DAH-SQ** has preferential access to cancer cells, which possess considerably more negative membrane potential, through the SIT property.[26] These results indicate that the nanoprobe **IMC-DAH-SQ** could highly selectively light up and distinguish cancer cells over normal cells with a high contrast ratio.

COX-2 inhibition experiment

To further confirm that the nanoprobe **IMC-DAH-SQ** does target COX-2 in cancer cells, control experiments were performed. Cancer cells (MCF-7, A549 and HepG2) were preincubated with the potent COX-2 inhibitors celecoxib (CXB) or IMC, followed by the addition of **IMC-DAH-SQ**.[27] As expected, **IMC-DAH-SQ** could

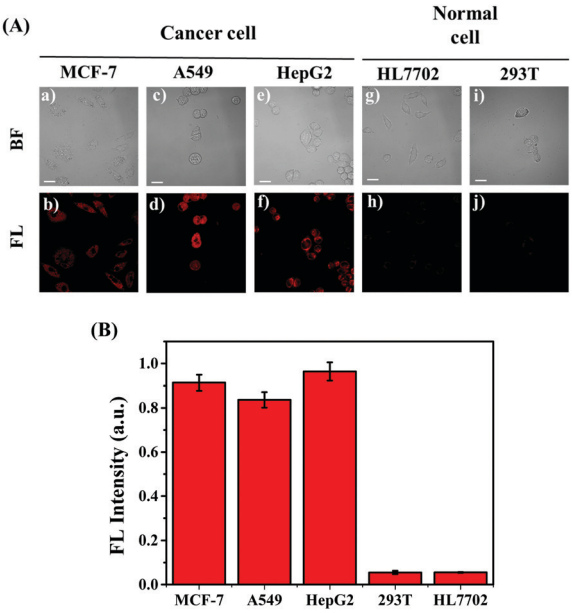

Fig. 4 (A) The confocal laser scanning microscope imaging of different cell lines stained with 5 μM nanoprobe **IMC-DAH-SQ**. a, c, e, g and i present bright light images, and b, d, f, h and j present fluorescence images. Scale bar: 20 μm; (B) quantitative analysis of the fluorescence signal of **IMC-DAH-SQ**. The excitation wavelength nanoprobe is 635 nm and the scanning range is 645–700 nm.

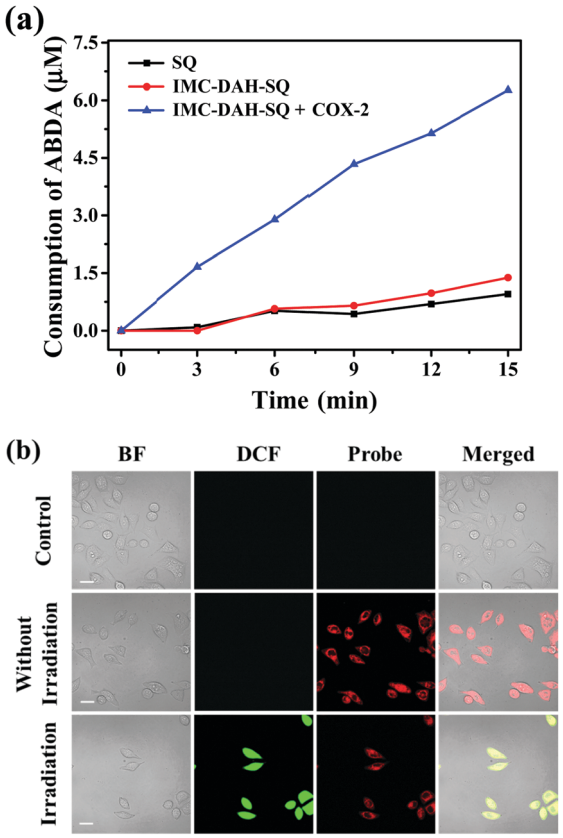

Fig. 5 (a) Consumption of 50 μM ABDA upon mixing with 5 μM SQ, 5 μM **IMC-DAH-SQ** with and without COX-2 under irradiation at a power density of 25 mW cm^{-2} for different times. (b) The experiment of detecting intracellular ROS production in HepG2 cells. HepG2 cancer cells upon incubation with 5 μM **IMC-DAH-SQ** and 10 μM DCFH-DA for 0.5 h, imaged after light illumination (25 mW cm^{-2}, 12.5 min, 630 nm). Scale bar: 20 μm.

not target these cancer cells, and no obvious fluorescence was observed (Fig. S5, ESI†). The nanoparticles of **IMC-DAH-SQ** remained in a state of aggregation because the COX-2 receptors that were occupied by competitive inhibitors lost the capability of binding **IMC-DAH-SQ**.

Lipopolysaccharide up-regulates COX-2 levels

Although SIT can improve the uptake of **IMC-DAH-SQ** by tumor cells, it cannot disaggregate the nanoprobes to produce fluorescence. To further prove that the NIR turn-on fluorescence enhancement arose from COX-2 interactions, we observed the fluorescence changes after normal intracellular COX-2 was upregulated by lipopolysaccharide (LPS).[28] As shown in Fig. S6 (ESI†), as the normal cells were preincubated with LPS for 12 h, an enhanced fluorescence signal was observed. Undoubtedly, the turn-on fluorescence response came from the nanoprobe disaggregate induced by the interaction with COX-2. The nanoprobe **IMC-DAH-SQ** can distinguish cancer cells by monitoring COX-2 levels in living systems.

ROS detection *in vitro*

After proving that nanoprobe **IMC-DAH-SQ** can identify cancer cells by overexpression of COX-2, we studied whether the nanoprobe *in vitro* can produce ROS by using ABDA as a ROS indicator.[29] As expected, the **IMC-DAH-SQ** binding with COX-2 has a strong ROS productivity that is higher than that of free SQ and **IMC-DAH-SQ** (Fig. S7, ESI†). As shown in Fig. 5a, the consumption of ABDA was calculated to be 6.26 μM in the presence of COX-2 upon irradiation for 15 min, while that of **IMC-DAH-SQ** was 1.38 μM and that of SQ was 0.95 μM at the same time. This result indicates that the presence of COX-2 enables the nanoprobe to more readily disaggregate and is more conducive to producing ROS. The singlet oxygen quantum yields of **IMC-DAH-SQ** in the absence and presence of COX-2 were 5.7×10^{-3} and 0.035, respectively (Fig. S8 and Table S1, ESI†). COX-2 overexpressed in tumor cells triggers 6-fold enhancement of the singlet oxygen quantum yield, showing the good tumor-adaptive PDT outcome of **IMC-DAH-SQ**. It is promising that the nanoprobe would have strong ROS generation ability in tumor cells and possess significant advantages in the ablation of tumor cells.

Intracellular ROS detection

2′,7′-Dichlorodihydrofluorescein diacetate (DCFH-DA), a well-known ROS indicator, was employed to investigate the intracellular ROS production.[30] As shown in Fig. 5b, HepG2 cells preincubated with **IMC-DAH-SQ** showed NIR fluorescence, indicating that **IMC-DAH-SQ** accumulated well in the cells through endocytosis. Without irradiation, no green emission was observed. In contrast, a bright green fluorescence signal

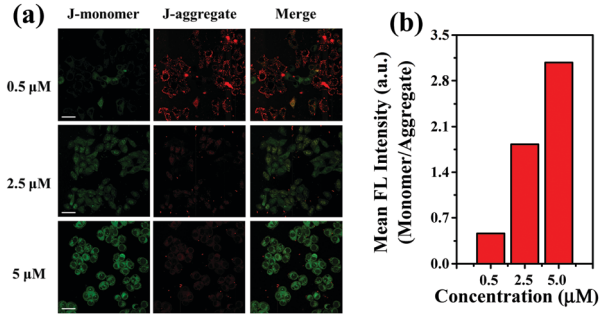

Fig. 6 (a) Confocal images of the mitochondrial membrane potential probe JC-1 and (b) mean fluorescence intensity of the monomer/aggregate in HepG2 cells treated with different concentrations of the nanoprobe **IMC-DAH-SQ** after irradiation. The excitation wavelength of JC-1 monomer is 488 nm and the scanning range is 500–540 nm; the excitation wavelength of JC-1 aggregate is 561 nm and the scanning range is 570–610 nm. Scale bar: 20 μm.

was detected after irradiation, confirming the **IMC-DAH-SQ** capability of producing intracellular ROS.

Co-localization experiments and mitochondrial membrane potential detection

After cancer cells were incubated with **IMC-DAH-SQ**, red fluorescence was evenly distributed in the cytoplasm. Increasing evidence shows that SQ derivatives can target mitochondria preferentially,[31] and given the characteristics of the positively charged surface of the nanoparticles (37.8 mV), **IMC-DAH-SQ** may be mainly accumulated in the mitochondria of cells. To study the subcellular distribution of **IMC-DAH-SQ**, the commercial mitochondrial probe Rhodamine 123 was used for colocalization (Fig. S9, ESI†). As expected, the fluorescence of the nanoprobe **IMC-DAH-SQ** overlaps well with that of Rhodamine 123 (the Pearson's coefficient is as high as 0.96), which proves that the nanoprobe **IMC-DAH-SQ** can accumulate in mitochondria. As the energy center of cells, mitochondria are more susceptible to toxic ROS than other subcellular organelles.[15] Therefore, ROS production in mitochondria is more likely to induce the death of cells. The decrease of the mitochondrial membrane potential (MMP) is considered to be the first event in the apoptosis cascade. The fluorescence change of the probe JC-1 can be used to observe the decrease of MMP.[13] As shown in Fig. 6, with increasing concentration of **IMC-DAH-SQ**, the red fluorescence signal assigned to J-aggregates of JC-1 slowly reduced, while the green fluorescence signal of the monomers gradually increased. The increased monomer/aggregate ratio further proves that PDT of **IMC-DAH-SQ** destroys the cell mitochondria, leading to the depolarization of MMP and damage to the cancer cells.

Photodynamic therapy

Before studying the PDT capability of the probe **IMC-DAH-SQ** to cancer cells, we measured the cell survival rates of different groups (IMC, SQ, IMC/SQ mixture and **IMC-DAH-SQ**) treated with varying concentrations with or without irradiation using MTT assays. As shown in Fig. 7, without irradiation, the survival rates of these groups are close to 100%. Upon irradiation, the survival rate of cells pretreated with **IMC-DAH-SQ** decreased

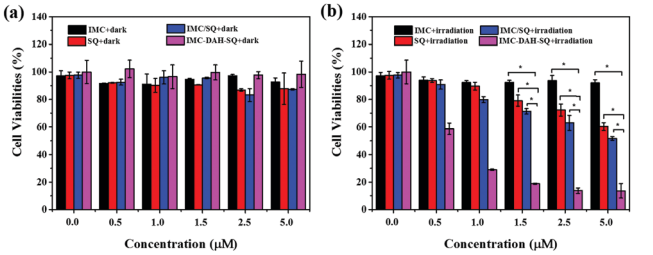

Fig. 7 (a and b) The cell viabilities of different concentrations of IMC, SQ, IMC/SQ mixture and **IMC-DAH-SQ** with different irradiation conditions. $^*P < 0.05$.

significantly with increasing concentration. With 25 mW cm^{-2}, the half-maximal inhibitory concentration (IC_{50}) of **IMC-DAH-SQ** was 0.59 μM. Still, the data were as high as 5.02 and 7.40 μM for the IMC/SQ mixture and SQ, respectively, suggesting significantly increased PDT capability of **IMC-DAH-SQ** by about 10-fold. Together with these results, we can find that **IMC-DAH-SQ** showed remarkable inhibition of cell growth.

To further clarify the PDT effect of the probe **IMC-DAH-SQ** on cancer cells under light radiation, we compared the inhibition of the probe with the control group through the calcein-AM/PI staining experiment. Under the same experimental conditions, the inhibition ability of **IMC-DAH-SQ** to cancer cells was stronger than that of the control groups (SQ, IMC/SQ) (Fig. S10, ESI†). Although SQ alone possesses the SIT property, which can enable SQ molecules to target cancer cells independently, SQ molecules cannot effectively generate ROS to ablate cancer cells under irradiation due to the ACQ effect. However, for **IMC-DAH-SQ**,

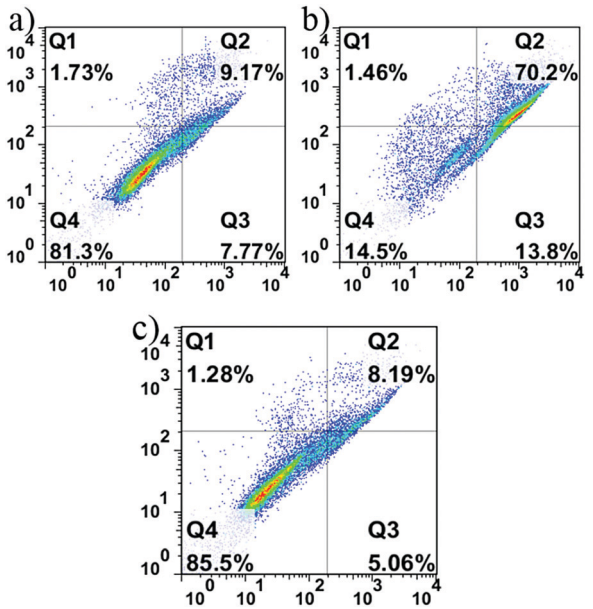

Fig. 8 Flow cytometry results measured by the fluorescence intensity of Annexin V-FITC and PI to identify cell health (Q1: necrotic cells, Q2: late apoptotic cells, Q3: early apoptotic cells, Q4: normal cells). (a) and (b) Represent the cells in the presence of **IMC-DAH-SQ** without and with laser irradiation; (c) the cells in the absence of **IMC-DAH-SQ** with laser irradiation.

in addition to the SIT function, the specific binding of IMC and COX-2 is conducive not only to targeting cancer cells but also to subsequent disaggregation of the probe molecules. Under this condition, the existing SQ monomer segment can effectively generate ROS and achieve PDT. Therefore, the PDT efficiency of **IMC-DAH-SQ** is significantly more robust than that of the control groups, mainly due to the advantages of the molecular design of **IMC-DAH-SQ**, which include multiple targeting ability and the controllable PDT induced by tumor cell microenvironmental COX-2. To further investigate the proportion of cell death treated by **IMC-DAH-SQ**, flow cytometry was used to detect the degree (Fig. 8). The results showed that **IMC-DAH-SQ** caused a significant increase in the cell apoptosis rate (from 8.19% to 70.2%) and no obvious change in the necrosis rate (less than 2%). Apoptosis is the main mode of tumor cell death triggered by the PDT of **IMC-DAH-SQ**.

Conclusions

In summary, we have designed and synthesized a novel molecule, **IMC-DAH-SQ**, which can self-assemble into nanoprobes. Depending on its SIT ability and the specific interaction between IMC and the highly expressed COX-2 in tumor cells, the nanoprobe can light up and identify cancer cells with high selectivity and a NIR signal-to-noise ratio. The disaggregation of the nanoprobe initiated by COX-2 and the notable accumulation in mitochondria endows the molecule with PDT activity and imaging-guided PDT potential in tumor cells. The tumor targeting turn-on fluorescent probe with photodynamic therapy activity for COX-2 overexpressed cancer cells provides a new platform for tumor cell diagnosis and promising PDT treatment, opening a new avenue of molecular design for imaging-guided PDT.

Conflicts of interest

There are no conflicts to declare.

Acknowledgements

This work was supported by the National Natural Science Foundation of China (Grant No. 21978241, 21676218, and 21878249) and Shaanxi Province Science and Technology (2019JM-173 and 2018JM2008).

Notes and references

1 Z. Zhou, J. Song, L. Nie and X. Chen, *Chem. Soc. Rev.*, 2016, **45**, 6597–6626.
2 H. Abrahamse and M. R. Hamblin, *Biochem. J.*, 2016, **473**, 347–364.
3 J. Liu, T. Liu, P. Du, L. Zhang and J. Lei, *Angew. Chem., Int. Ed.*, 2019, **58**, 7808–7812.
4 L. Sun, Y. Xu, Y. Gao, X. Huang, S. Feng, J. Chen, X. Wang, L. Guo, M. Li, X. Meng, J. Zhang, J. Ge, X. An, D. Ding, Y. Luo, Y. Zhang, Q. Jiang and X. Ning, *Small*, 2019, **15**, 1901156.
5 M. Jahanshahi, E. Kowsari, V. Haddadi Asl, M. Khoobi, J. H. Lee, F. B. Kadumudi, S. Talebian, N. Kamaly and M. Mehrali, *Int. J. MediPharm Res.*, 2019, **572**, 118791.
6 J. Zhao, S. Wu, J. Qin, D. Shi and Y. Wang, *ACS Appl. Mater. Interfaces*, 2018, **10**, 41986–41998.
7 M. Li, T. Xiong, J. Du, R. Tian, M. Xiao, L. Guo, S. Long, J. Fan, W. Sun, K. Shao, X. Song, J. W. Foley and X. Peng, *J. Am. Chem. Soc.*, 2019, **141**, 2695–2702.
8 M. H. Park, G. Jo, E. J. Kim, J. S. Jung and H. Hyun, *Chem. Commun.*, 2020, **56**, 4180–4183.
9 E. A. Owens, S. Lee, J. Choi, M. Henary and H. S. Choi, *Wiley Interdiscip. Rev.: Nanomed. Nanobiotechnol.*, 2015, **7**, 828–838.
10 Y. Zheng, V. Comaills, R. Burr, G. Boulay, D. T. Miyamoto, B. S. Wittner, E. Emmons, S. Sil, M. W. Koulopoulos, K. T. Broderick, E. Tai, S. Rengarajan, A. S. Kulkarni, T. Shioda, C. L. Wu, S. Ramaswamy, D. T. Ting, M. Toner, M. N. Rivera, S. Maheswaran and D. A. Haber, *Proc. Natl. Acad. Sci. U. S. A.*, 2019, **116**, 5223–5232.
11 S. Xu, M. J. Uddin, S. Banerjee, K. Duggan, J. Musee, J. R. Kiefer, K. Ghebreselasie, C. A. Rouzer and L. J. Marnett, *J. Biol. Chem.*, 2019, **294**, 8690–8698.
12 S. Fulda, L. Galluzzi and G. Kroemer, *Nat. Rev. Drug Discovery*, 2010, **9**, 447–464.
13 C. Liu, B. Liu, J. Zhao, Z. Di, D. Chen, Z. Gu, L. Li and Y. Zhao, *Angew. Chem., Int. Ed.*, 2020, **59**, 2634–2638.
14 S. E. Weinberg and N. S. Chandel, *Nat. Chem. Biol.*, 2010, **9**, 447–464.
15 H. S. Jung, J. H. Lee, K. Kim, S. Koo, P. Verwilst, J. L. Sessler, C. Kang and J. S. Kim, *J. Am. Chem. Soc.*, 2017, **139**, 9972–9978.
16 E. A. Owens, H. Hyun, T. L. Dost, J. H. Lee, G. Park, D. H. Pham, M. H. Park, H. S. Choi and M. Henary, *J. Med. Chem.*, 2016, **59**, 5311–5323.
17 J. H. Shi, T. R. Wang, Y. Q. You, M. L. Akhtar, Z. J. Liu, F. Han, Y. Li and Y. Wang, *Nanoscale*, 2019, **11**, 13078–13088.
18 S. Singh, A. Aggarwal, N. V. Bhupathiraju, G. Arianna, K. Tiwari and C. M. Drain, *Chem. Rev.*, 2015, **115**, 10261–10306.
19 Y. Xu, A. Malkovskiy and Y. Pang, *Chem. Commun.*, 2011, **47**, 6662–6664.
20 M. J. Uddin, B. C. Crews, K. Ghebreselasie and L. J. Marnett, *Bioconjugate Chem.*, 2013, **24**, 712–723.
21 X. Fan, Q. He, S. Sun, H. Li, Y. Pei and Y. Xu, *Chem. Commun.*, 2016, **52**, 1178–1181.
22 S. Xu, M. J. Uddin, S. Banerjee, K. Duggan, J. Musee, J. R. Kiefer, K. Ghebreselasie, C. A. Rouzer and L. J. Marnett, *J. Biol. Chem.*, 2019, **294**, 8690–8698.
23 N. Adarsh, R. R. Avirah and D. Ramaiah, *Org. Lett.*, 2010, **12**, 5720–5723.
24 C. Zhang, T. Liu, Y. Su, S. Luo, Y. Zhu, X. Tan, S. Fan, L. Zhang, Y. Zhou, T. Cheng and C. Shi, *Biomaterials*, 2010, **31**, 6612–6617.
25 H. Zhang, J. Fan, J. Wang, B. Dou, F. Zhou, J. Cao, J. Qu, Z. Cao, W. Zhao and X. Peng, *J. Am. Chem. Soc.*, 2013, **135**, 17469–17475.

26 M. Li, S. Long, Y. Kang, L. Guo, J. Wang, J. Fan, J. Du and X. Peng, *J. Am. Chem. Soc.*, 2018, **140**, 15820–15826.
27 H. S. Kim, T. Park, W. X. Ren, J.-Y. Lim, M. Won, J. S. Heo, S. G. Lee and J. S. Kim, *Dyes Pigm.*, 2018, **150**, 261–266.
28 M. J. Uddin, B. C. Crews, A. L. Blobaum, P. J. Kingsley, D. L. Gorden, J. O. McIntyre, L. M. Matrisian, K. Subbaramaiah, A. J. Dannenberg, D. W. Piston and L. J. Marnett, *Cancer Res.*, 2010, **70**, 3618–3627.
29 L. Shao, Y. Pan, B. Hua, S. Xu, G. Yu, M. Wang, B. Liu and F. Huang, *Angew. Chem., Int. Ed.*, 2020, **59**, 11779–11783.
30 C. Zhang, F. Gao, W. Wu, W. X. Qiu, L. Zhang, R. Li, Z. N. Zhuang, W. Yu, H. Cheng and X. Z. Zhang, *ACS Nano*, 2019, **13**, 11249–11262.
31 M. Dichiara, O. Prezzavento, A. Marrazzo, V. Pittala, L. Salerno, A. Rescifina and E. Amata, *Eur. J. Med. Chem.*, 2017, **142**, 459–485.